The 2010 IEEE/RSJ International Conference on
Intelligent Robots and Systems
October 18-22, 2010, Taipei, Taiwan

Daytime Water Detection Based on Color Variation

Arturo Rankin and Larry Matthies

Abstract—**Robust water detection is a critical perception requirement for unmanned ground vehicle (UGV) autonomous navigation. This is particularly true in wide open areas where water can collect in naturally occurring terrain depressions during periods of heavy precipitation and form large water bodies (such as ponds). At far range, reflections of the sky provide a strong cue for water. But at close range, the color coming out of a water body dominates sky reflections and the water cue from sky reflections is of marginal use. We model this behavior by using water body intensity data from multiple frames of RGB imagery to estimate the total reflection coefficient contribution from surface reflections and the combination of all other factors. We then describe an algorithm that uses one of the color cameras in a forward-looking, UGV-mounted stereo-vision perception system to detect water bodies in wide open areas. This detector exploits the knowledge that the change in saturation-to-brightness ratio across a water body from the leading to trailing edge is uniform and distinct from other terrain types. In test sequences approaching a pond under clear, overcast, and cloudy sky conditions, the true positive and false negative water detection rates were (95.76%, 96.71%, 98.77%) and (0.45%, 0.60%, 0.62%), respectively. This software has been integrated on an experimental unmanned vehicle and field tested at Ft. Indiantown Gap, PA, USA.**

I. Introduction

Detecting water hazards is a significant challenge to unmanned ground vehicle (UGV) autonomous navigation over cross country terrain. This is particularly true for military UGVs navigating over wide open areas such as clearings. Here, higher vehicle speeds are desired when executing tactical behaviors such as "dash to cover". But these are areas that typically contain some naturally occurring depressions where large water bodies (such as ponds) can form during periods of heavy precipitation. The probability of driving into a water hazard increases when a UGV is required to operate at higher than normal speeds, especially since *a priori* water data may not be available as current water hazards may not have existed when the most recent digital terrain map was generated. Thus, the need to traverse wide open areas at high speed while detecting and avoiding previously unknown water traps necessitates robust water detection.

Water detection for UGV autonomous navigation is still a relatively new research area. In 2003, Matthies et al. [1] cataloged the environmental variables affecting the properties and conditions of surface water, and discussed the sensors applicable to detecting it under each condition. Iqbal et al. [2] recently performed a survey of sensors and algorithms applicable to water detection.

Both passive sensors {visible, short-wave infrared (SWIR), thermal infrared (TIR), polarization, hyperspectral [1][3][4][5][6]} and active sensors (laser [7][8]) have been explored for water detection. Although laser sensors often get no return value on free-standing water [7], fusing laser cues for water with color cues for water can increase water detectability [8]. But because there are military operations when it may be desirable for UGVs to operate without emitting strong, detectable electromagnetic signals, a passive perception solution to water detection is desirable.

Polarization cameras have been successfully used by several researchers to detect water bodies [3][4][5]. However, polarization cameras (as well as SWIR, TIR and hyperspectral sensors) are relatively high cost in comparison to visible sensors. In order to accurately transfer water detection results from one of these specialized cameras to a terrain map used to plan safe paths, either a second specialized camera or a pair of visible cameras are required to perform stereo ranging, or a separate ranging sensor (such as a 3D laser scanner) is required.

Low cost visible cameras have also been successfully used to detect water bodies [1][9][10][11][12]. The appearance of water can greatly vary, depending upon the color of the sky, the level of turbidity, the time of day, and the presence of wind, terrain reflections, underwater objects visible from the surface, surface vegetation, and shadows. The large number of possible scenarios and appearances of water makes water detection particularly challenging using a single cue. A single cue for water tends to only be reliable under certain conditions. For example, spatiotemporal variation analysis is useful in detecting moving water from a stationary platform, but not still water [13]. In [9] and [11], multiple cues for water from visible cameras were fused. In [1], a supervised RGB classifier based on a mixture of Gaussians model was used, and in [12], active learning and mean-shift based image segmentation were combined.

Manuscript received March 10, 2010. The research described in this paper was carried out by the Jet Propulsion Laboratory (JPL), California Institute of Technology, and was sponsored by the U. S. Army Research Laboratory (ARL) under the RCTA program through an agreement with the National Aeronautics and Space Administration. Reference herein to any specific commercial product, process, or service by trademark, manufacturer, or otherwise, does not constitute or imply its endorsement by the United States Government or JPL, California Institute of Technology.

A. Rankin is with the Jet Propulsion Laboratory, California Institute of Technology, Pasadena, CA 91109 USA. (phone: 818-354-9269; fax: 818-393-5007; e-mail: Arturo.Rankin@ jpl.nasa.gov).

L. Matthies is with the Jet Propulsion Laboratory, California Institute of Technology, Pasadena, CA 91109 USA. (phone: 818-354-3722).

However, both of these methods require manual labeling of sample imagery prior to autonomous navigation.

Under the Robotics Collaborative Technology Alliances (RCTA) program, we have developed a water detector for wide-open areas that uses a forward-looking stereo pair of color cameras mounted to the front of a UGV to detect water bodies at mid to far range, where reflections of the sky provide a strong cue for water. We have demonstrated the detection and localization of large water bodies at ranges beyond 50 meters with our sky reflection detector [14]. However, we cannot rely on only detecting water bodies in wide open areas when they are far away. An autonomous vehicle operating on challenging terrain will often suddenly change its heading, causing water bodies to come in and out of a sensor's field of view at any range.

At close range, the color coming out of a water body dominates sky reflections and the water cue from sky reflections is of marginal use. In section III, we model this behavior by using water body intensity data from multiple frames of RGB imagery to estimate the total reflection coefficient contribution from surface reflections and the combination of all other factors. In section IV, we describe an algorithm that uses one of the color cameras in a forward-looking, UGV-mounted stereo-vision perception system to detect water bodies in wide open areas. This detector exploits the knowledge that the change in saturation-to-brightness ratio across a water body from the leading to trailing edge is uniform and distinct from other terrain types. While this detector only uses a single color camera to classify water, stereo processing (which is beyond the scope of this paper) is performed to localize detected water in a terrain map.

II. Multi-Frame Water Segmentation

In this section, we describe a technique used for segmenting portions of water bodies for color analysis. This technique was applied to the water body described in Fig. 1 in order to obtain image intensity data on a large set of water pixels from multiple frames. The intensity data was used to experimentally develop a model of the reflection coefficients from the water body in Fig. 1. Fig. 1 contains an RGB image of a long water body (>50 meters) and hue, saturation, and brightness (HSB) color components. The leading edge is close to the UGV and the trailing edge is far away. Sky reflections dominate near the trailing edge but have a significantly reduced effect on the perceived color of the water near the leading edge. The sequence of images leading up to this water body starts 40 meters from the water's leading edge. The frame in Fig. 1 is near the end of a 143 frame sequence.

As illustrated in the Fig. 1 brightness image, water bodies tend to have a uniform brightness where they are not reflecting objects. Thus, low texture can be a cue for water. To locate regions of low texture, we convert the native RGB images to grayscale and pass a 5x5 intensity variance filter over the grayscale images. In the sample intensity variance image in Fig. 1, red corresponds to low variance, blue corresponds to high variance, and the colors in between correspond to an intermediate variance. Here, variance is only calculated for pixels with a grayscale intensity above 100 (on a 0-225 scale).

The rational for ignoring the variance of low intensity regions is that we do not expect water to be extremely dark during the daytime in imagery from a sensor sensitive to the visible spectrum. Using a cutoff intensity limits the search space for candidate water bodies. In this case, however, a portion of the water body in the foreground is below the cutoff intensity. We detect that region by expanding the low intensity variance region to include neighboring pixels that have a low intensity gradient.

The majority of this water body was segmented in every frame of the sequence by performing a union of the region near the trailing edge strongly reflecting the sky, low intensity variance regions, and low intensity gradient regions. Stereo range data was used to project water pixels into a digital terrain map having a resolution of 0.4 meters. For the 143 frame sequence, 23,731 map cells were segmented as water, an average of 159 cells from each frame. For each map cell segmented as water, the angle between the ray from the cell center to the left camera focal plane array and zenith (i.e., the angle of incidence) and the average color in each cell was used to develop an empirical model of water reflection coefficients.

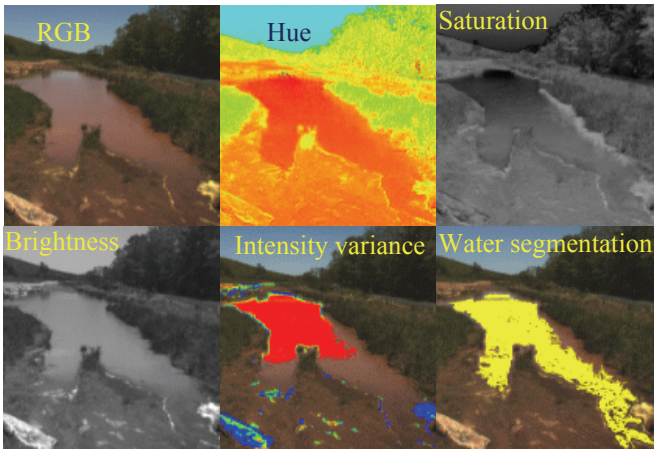

Fig. 1. A frame near the end of a 143 frame sequence containing a long water body. The majority of the water pixels in this sequence was segmented in software by performing a union of the region near the trailing edge strongly reflecting the sky, low intensity variance regions, and low intensity gradient regions.

III. Model of Water Reflection Coefficients

When electromagnetic energy reaches a water surface, it can be reflected off the surface, transmitted into the water, absorbed by the water, scattered by the water, absorbed by materials suspended in the water, reflected or scattered by materials suspended in the water, and reflected off the bottom of the water. Deriving a full model of the energy flux from water bodies would be fairly difficult. As an

alternative, we use experimental data to develop a partial model of the reflection coefficients.

The total reflection coefficient R_{total} from a water body to a camera is the sum of the reflection coefficients for energy reflected off the water surface to the camera R_r, scattered by water molecules to the camera R_p, reflected or scattered by materials suspended in the water to the camera R_s, and reflected off the bottom of the water to the camera R_b (1). The fraction of the incident power that is reflected from an air/water interface is given by Fresnel equations (2) and (3) for light polarized perpendicular to and parallel to the plane of incidence, where n_1 is the refractive index of air, n_2 is the refractive index of water, and θ is the angle of incidence.

The refractive index of air and pure water is 1.03 and 1.33, respectively. The most significant factors that can affect the refractive index of water are the wavelength of the light entering it and its salinity. However, these factors only alter the refractive index of water by as much as 1%. For unpolarized incident light, such as would be present on overcast days, the fraction of the incident power that is reflected from an air/water interface is the average of the polarized reflection coefficients (4). As illustrated in Fig. 2, the energy reflected off the surface of water bodies increases with increasing incidence angle. For this work, we make the assumptions that, for the purpose of estimating the surface reflection coefficient for water bodies, the refractive index for pure water can be used and the incident light is mostly unpolarized.

$$R_{total} = R_r + R_p + R_s + R_b \tag{1}$$

$$R_{r,\perp}(\theta) = \left[\frac{n_1 \cos\theta - n_2 \sqrt{1 - \left(\frac{n_1}{n_2} \sin\theta \right)^2}}{n_1 \cos\theta + n_2 \sqrt{1 - \left(\frac{n_1}{n_2} \sin\theta \right)^2}} \right]^2 \tag{2}$$

$$R_{r,\parallel}(\theta) = \left[\frac{n_1 \sqrt{1 - \left(\frac{n_1}{n_2} \sin\theta \right)^2} - n_2 \cos\theta}{n_1 \sqrt{1 - \left(\frac{n_1}{n_2} \sin\theta \right)^2} + n_2 \cos\theta} \right]^2 \tag{3}$$

$$R_r(\theta) = \frac{R_{r,\perp}(\theta) + R_{r,\parallel}(\theta)}{2} \tag{4}$$

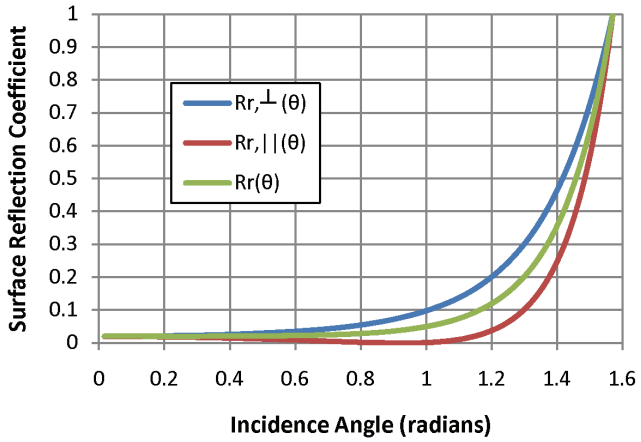

Fig. 2. Theoretical fraction of incident power that is reflected from an air/pure water interface as a function of incidence angle. $R_{r,\perp}(\theta)$ and $R_{r,\parallel}(\theta)$ are the Fresnel reflection coefficients for light polarized perpendicular to and parallel to the plane of incidence, respectively. $R_r(\theta)$ is the Fresnel reflection coefficient for unpolarized light.

Thus far, we have an expression for the surface reflection coefficient R_r in (1). Rather than model each of the remaining reflection coefficients in (1), we combine the reflection coefficients for energy scattered by the water R_p, reflected or scattered by materials suspended in the water R_s, and reflected off the bottom of the water R_b into a single term R_o (5). The intensity values of water pixels are related to the total reflection coefficient by (6), where L is an illumination factor. Illumination depends on solar incidence angle, sky conditions, and terrain topology. Since the duration of the data collection on the water body in Fig. 1 was relatively short (~1 minute) and the water body is in an open area where few shadows are cast on the water, we assume constant illumination factor L. Substituting our simplified expression for R_{total} into (6) yields the expression in (7).

As shown in (8), the native RGB imagery is converted to grayscale (by averaging the RGB components) so that there is a single intensity value for each pixel. Fig. 3 contains a scatter plot of the grayscale intensity values on the water body in the image sequence described in Fig. 1. The intensity data is fairly linear and modeled using a least squares line fit (9). Recall that at high incidence angles, the surface reflection coefficient dominates the other reflection coefficients. Assuming $R_o(\theta)$ is negligible for an incidence angle of $\pi/2$, we can estimate the illumination factor L (10).

Finally, with an estimate of the illumination factor, a model of the intensity as a function of incidence angle, and an expression to calculate the surface reflection coefficient, we can estimate the sum of the remaining reflection coefficients in our model (11). Fig. 4 contains a plot of the surface reflection coefficient $R_r(\theta)$, the combination of the remaining reflection coefficients $R_o(\theta)$, and the modeled intensity as a function of the incidence angle θ. These

parameters can be cast in terms of the distance along flat ground D by using $D=H*tan(\theta)$, where H is the sensor height above the ground. For the data sets analyzed in this paper, the sensor height was 1.5 meters. Fig. 5 contains a plot of the surface reflection coefficient $R_r(\theta)$, the combination of the remaining reflection coefficients $R_o(\theta)$, and the modeled intensity as a function of the distance along the ground D. This model predicts that reflections of the sky dominate the perceived color of the water beyond ~12 meters.

$$R_{total} = R_r + R_o, \text{ where } R_o = R_p + R_s + R_b \quad (5)$$

$$I = LR_{total} \quad (6)$$

$$I_{pixel} = L\left[R_r(\theta) + R_o(\theta)\right] \quad (7)$$

$$I_{pixel} = \left[(red + green + blue)/3\right]/255 \quad (8)$$

$$I_{pixel} \approx I_{model} = 0.443077\theta - 0.176678 \quad (9)$$

$$L \approx \frac{I_{model}(\pi/2)}{R_r(\pi/2)} \quad (10)$$

$$R_o(\theta) \approx \frac{I_{model}}{L} - R_r(\theta) \quad (11)$$

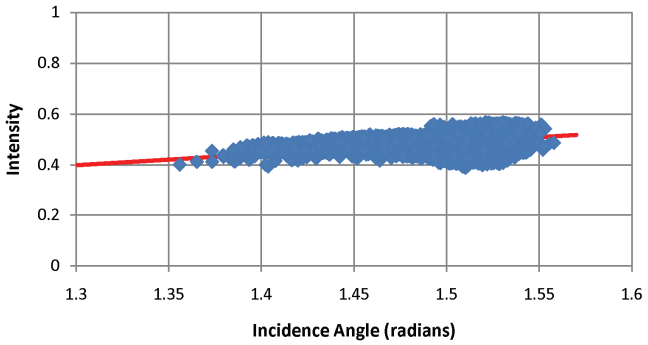

Fig. 3. The average of the RGB components for the water body in Fig. 1, plotted on a 0-1 scale, is used as a measure of intensity. The intensity values can be modeled with the line $I = 0.4431\theta - 0.1767$.

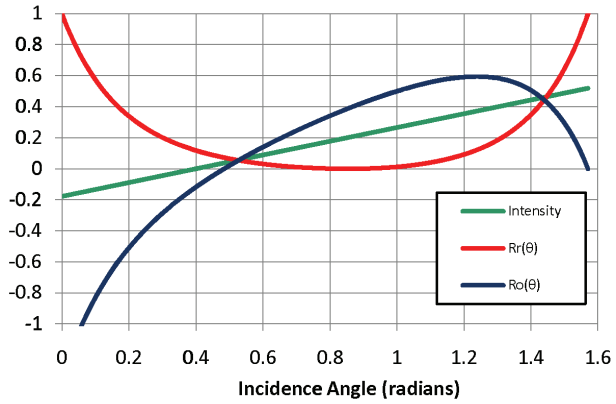

Fig. 4. Surface reflection coefficient $R_r(\theta)$, the combination of other the reflection coefficients $R_o(\theta)$, and modeled intensity ($I = 0.4431\theta - 0.1767$) as a function of incidence angle.

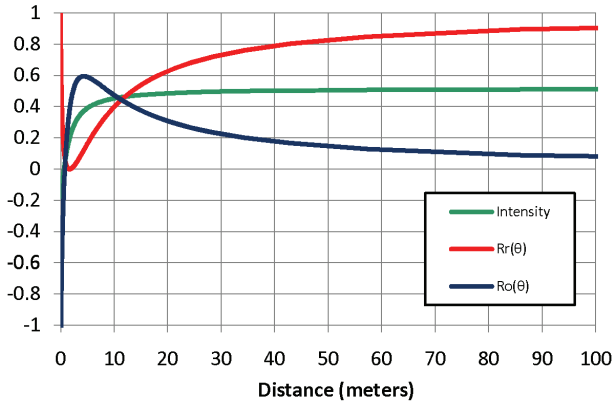

Fig. 5. Surface reflection coefficient $R_r(\theta)$, the combination of other the reflection coefficients $R_o(\theta)$, and modeled intensity as a function of the distance along the ground, given a sensor height of 1.5 meters above the ground.

IV. Water Detection

We have observed that the color of a water body tends to gradually change from the leading edge to the trailing edge, when other naturally occurring terrain types typically do not. In this section, we develop a method for detecting water bodies in wide-open areas based on their variation in color as a function of incidence angle. Fig. 6 contains a scatter plot of the average RGB and HSB color components for the 23,731 water map cells extracted from the sequence described in Fig. 1. Red, green, blue, brightness, and saturation values are plotted using a 0-255 scale, and hue is plotted using a 0-360 scale. The hue scale is angular with 0° and 360° being equivalent.

Several observations can be made. From the RGB plot, red, green, and blue water content decrease with decreasing incidence angle, green at a faster rate than red, and blue at a faster rate than green. From the HSB plot, the water brightness was largely unchanged except at lower incidence angles, where it begins to decrease at a low rate. Moving from higher to lower incidence angles, water saturation increases at a high rate and then levels off. At very high incidence angles the hue of the water body is somewhat

unpredictable, spanning the entire scale. There, water strongly reflects haze just above the horizon causing the saturation to be low. Hue is undefined for zero saturation and numerically ill-determined for low saturation. At lower incidence angles, water hue was fairly linear with low slope. Fig. 7 illustrates the water hue at the beginning, in the middle, and at the end of the sequence. We focus our attention on the ratio of water saturation to brightness, as those two components trend in opposite directions.

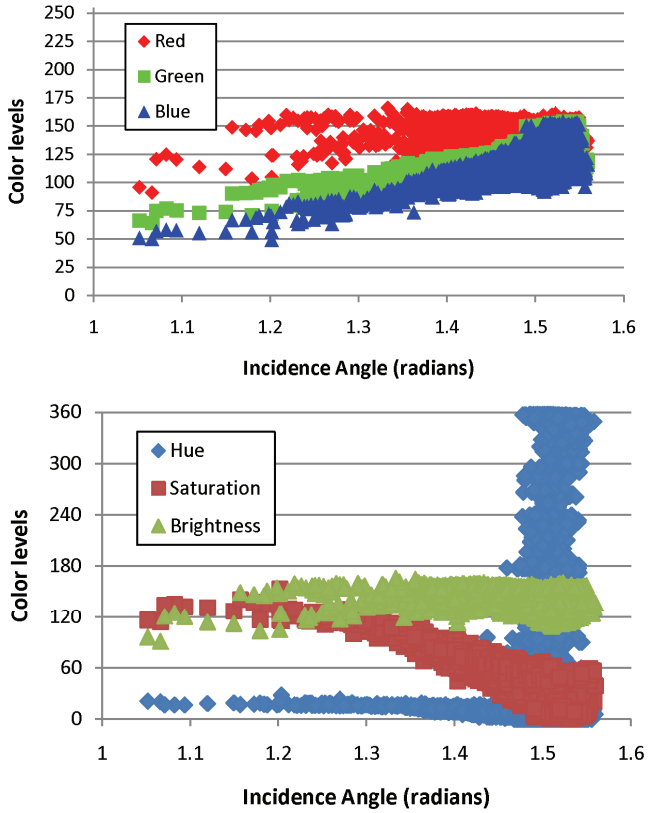

Fig. 6. A scatter plot of the RGB and HSB color components of the water body in Fig. 1 (as a function of angle of incidence) during a straight on approach starting from a range of 40 meters from the leading edge.

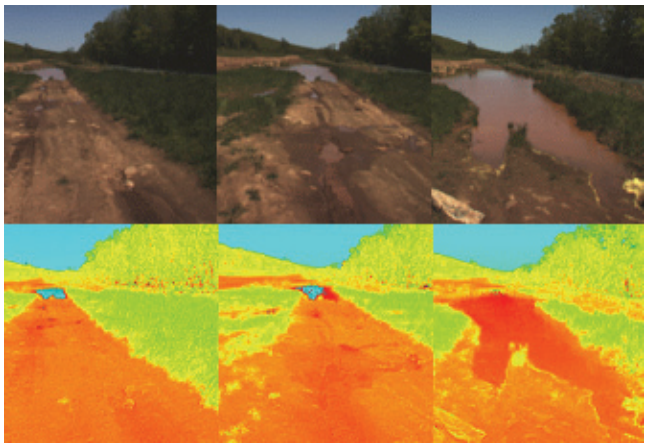

Fig. 7. As an open-area water body is approached, the sensed hue gradually changes from the hue of the sky to the hue coming out of the water.

Fig. 8 contains a plot of saturation divided by brightness as a function of incidence angle for the 23,731 water map cells extracted from the sequence described in Fig. 1. Note that the plot is fairly linear with high slope magnitude. (A brightness/saturation plot has a high positive slope.) As the water body is approached from a distance, the net change in brightness and saturation across the water body tends to increase. Fig. 9 shows plots of the maximum change in HSB color components over the water body in Fig. 1 for each frame in the sequence. The saturation content changes at a faster rate than the brightness content. We have implemented a water detector based on color variation that identifies candidate water regions in image space based on texture, evaluates the color changes across each candidate water region to locate those consistent with water, and performs filtering to prune regions that geometrically are not likely to be water. The steps in the algorithm are as follows:

a) In image space, low-texture regions with a monochrome intensity above some threshold and an average intensity much higher than their surrounds are identified as candidate water bodies.
b) Candidate water body regions are expanded using a flood fill algorithm that continues to add neighbor pixels as long as the intensity gradient in the brightness image is low.
c) An ellipse fit of each candidate water body is performed in image space.
d) A least-squares line fit of the pixels in each candidate water body is performed in brightness/saturation vs. incidence-angle space.
e) Assuming a horizontal ground plane at the front-wheel contact elevation, the pixel length and width of each ellipse are converted to meters.
f) The density of each candidate water region is calculated in image space in terms of the percentage of pixels in each ellipse that are candidate water pixels. Candidate water regions that are dense are more likely to be actual water regions. Low-density candidate water bodies tend to have a wireframe like appearance and are not likely water.
g) For each candidate water region, the line fit slope and average error, the ellipse aspect ratio, the blob size (in pixels), the blob density, and the blob length and width (in meters) are all thresholded.

Fig. 10 contains a water detection result for a single frame in the sequence. Each red ellipse contains a low texture region hypothesized to be water. After color variation and geometric filtering, only the ellipse containing yellow was ultimately detected as containing water. Fig. 11 shows the inclination angle of the least-squares line fit (step d) for true positive, true negative, false positive, and false negative water detection for each frame in the sequence. Water regions tend to have higher inclination angles than other naturally occurring terrain types. The false positive and false negative rates were both 1.4% for this sequence.

The water detector was run on three image sequences collected under clear, overcast, and cloudy sky conditions (see Fig. 12). The clear sky sequence was collected during an approach to the pond in Fig. 1 from 50 meters, and the overcast and cloudy sky sequences were collected during approaches to the same pond but from the opposite side (from 35 and 37 meters, respectively). For these sequences, a more aggressive inclination angle threshold of 1.25 radians was used. Table 1 contains water detection results for these three sequences.

Fig. 13 illustrates our color-variation based water detector outperforms our sky-reflection based water detector when water bodies are close to a UGV. Fig. 14 contains some additional examples of detecting close water bodies based on variation in color across low texture regions.

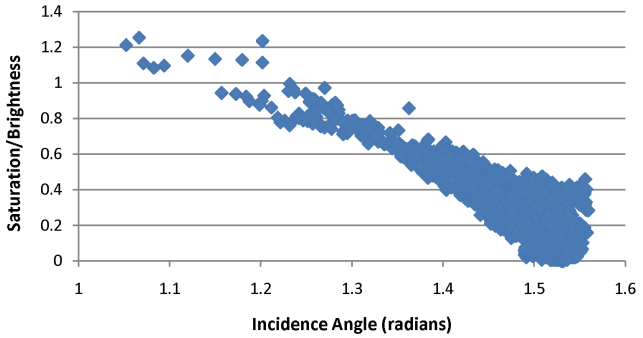

Fig. 8. A scatter plot of saturation/brightness (from the sequence described in Fig. 1) as a function of angle of incidence. Note that the plot is fairly linear with high slope magnitude. The slope magnitude appears to be higher for water than other naturally occurring terrain.

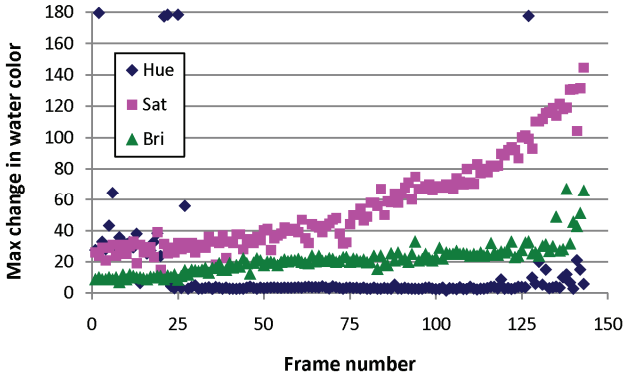

Fig. 9. The maximum change in HSB color components over the water body in Fig. 1 for each frame during a straight on approach starting from a range of 40 meters.

Fig. 10. A variety of characteristics are thresholded to detect water bodies based on color variation. Here, each red ellipse contains a single candidate water body. Only the one labeled yellow is ultimately detected as water.

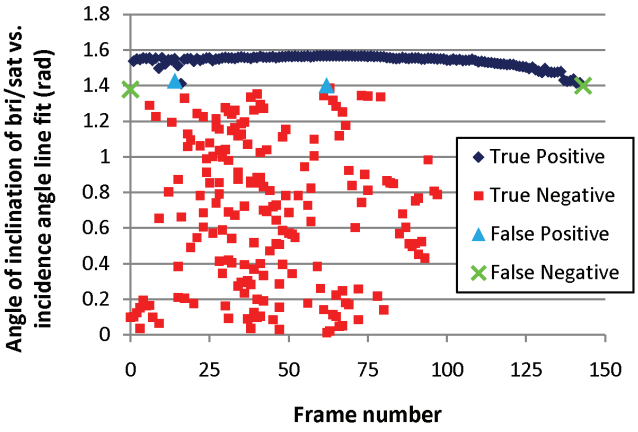

Fig. 11. Water detection results for the 143 frame sequence approaching the water body in Fig. 1. Each marker represents a candidate water body. An inclination angle threshold of 1.4 radians was used to classify low-texture blobs as water. The false positive and false negative rates were both 1.4%.

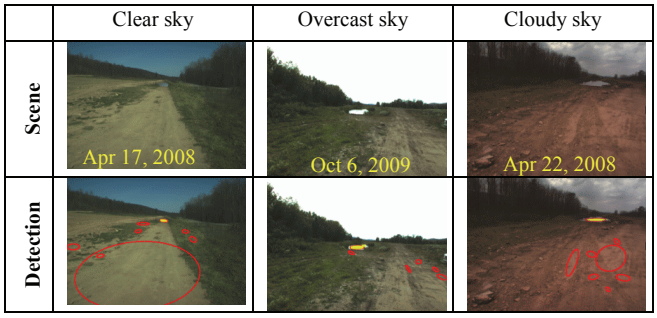

Fig. 12. First-frame water detection results for three sequences collected under clear, overcast, and cloudy sky conditions, approaching the water body in Fig. 1. The approaches on the overcast and cloudy days were from the opposite side.

Table 1. Water detection results for the 3 sequences illustrated in Fig. 12

Scene	1st frame distance to water	Num frames	True positive detection	False positive detection	Avg frame time
Clear	50 meters	237	227 (95.76%)	1 (0.45%)	128ms
Over-cast	35 meters	334	323 (96.71%)	2 (0.60%)	76ms
Cloudy	37 meters	162	160 (98.77%)	1 (0.62%)	54ms

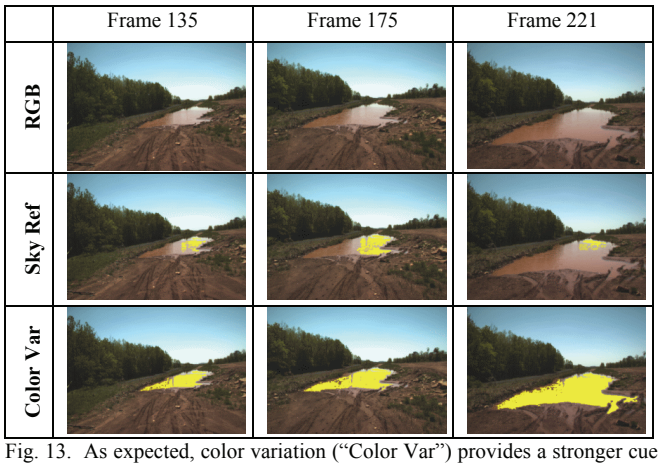

Fig. 13. As expected, color variation ("Color Var") provides a stronger cue for water than sky reflections ("Sky Ref") when the water body is close. Here, the water body in Fig. 1 was approached from the opposite side.

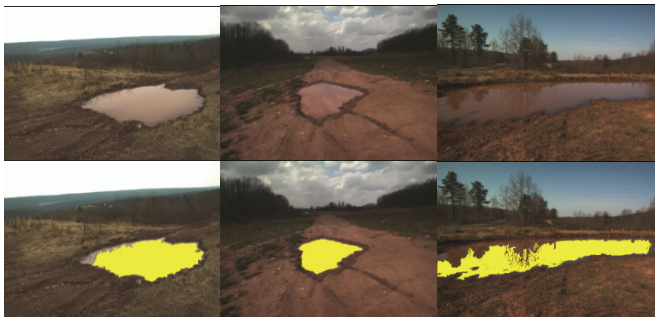

Fig. 14. Additional examples of detecting close water bodies based on color variation across low texture regions.

V. Conclusion

Robust water detection is a critical perception requirement for UGV autonomous navigation. Traversing through deep water bodies could cause costly damage to the electronics of UGVs. Additionally, a UGV that is either broken down due to water damage or stuck in a water body during an autonomous military mission may require rescue, potentially drawing critical resources away from the primary mission and soldiers into harm's way. In previous work, we developed software that detects water bodies out in the open at mid to far range, where sky reflections provide a strong cue for water. But at close range, the color coming out of a water body dominates sky reflections, and the water cue from sky reflections is of marginal use. A model of reflection coefficients developed using experimental water intensity data suggests that for a sensor height of 1.5 meters, sky reflections no longer dominate the color of water bodies at ranges less than ~12 meters.

We explored the possibility of developing a water detector based on the observation that the color of a water body tends to gradually change from the leading edge to the trailing edge, when other naturally occurring terrain types typically do not. Moving from higher to lower incidence angles, water body saturation and brightness move in opposite directions, with saturation increasing at a much higher rate than brightness decreases. For 23,731 water map cells segmented from a sequence of 143 frames approaching a water body starting at 40 meters, a plot of saturation/brightness vs. incidence angle is fairly linear with high slope magnitude. Fortuitously, the slope magnitude tends to be higher for water than other naturally occurring terrain, such as soil and vegetation. We have exploited this phenomenology to develop software that detects water bodies based on the variation in color across the water body.

First, we identify candidate water regions in image space by locating regions having low texture. Next, we evaluate the color changes across each candidate water region to locate those consistent with water. Finally, we perform an ellipse fit on remaining candidate water regions and apply some size and aspect ratio filtering to prune regions that geometrically are not likely to be water. In three color image sequences collected while approaching a pond on different days when the sky was clear, overcast, and cloudy (from starting distances of 50, 35, and 37 meters, respectively), the true positive and false negative water detection rates were (95.76%, 96.71%, 98.77%) and (0.45%, 0.60%, 0.62%), respectively. The average time to classify each 512x384 image on a 2.6 GHz Intel Core 2 Duo processor was 128, 76, and 54 milliseconds, respectively. The timing varies based on the number of low-texture regions segmented for classification.

Our practice is to run the sky reflection based water detector and the color variation based water detector in parallel to detect water bodies that are out in the open. These two detectors are complementary. The color variation based water detector performs well in detecting water bodies at close to mid range, and the sky reflection based detector performs well in detecting water bodies at mid to far range. These detectors have been integrated on an experimental unmanned vehicle and field tested at Ft. Indiantown Gap, PA [14].

References

[1] L. Matthies, P. Bellutta, and M. McHenry, "Detecting water hazards for autonomous off-road navigation," *Proceedings of SPIE*, Vol. 5083, Orlando, FL, pp. 231-242, April 2003.

[2] M. Iqbal, O. Morel, and F. Meriaudeau, "A survey of outdoor water detection," *The 5th International Conference on Information & Communication Technology and Systems (ICTS)*, Indonesia, 2009.

[3] A. Pandian, "Robot navigation using stereo vision and polarization imaging," Masters thesis, Institut Universitaire de Technologie IUT Le Creusot, Universit_e de Bourgogne, 2008.

[4] A. Sarwal, J. Nett, and D. Simon, "Detection of small water bodies," *PercepTek Robotics Technical Report*, Littleton, CO, (Available at: http://www.dtic.mil, AD# ADA433004), 2004.

[5] B. Xie, Z. Xiang, H. Pan, and J. Liu, "Polarization-based water hazard detection for autonomous off-road navigation," *Proceedings of the IEEE/RSJ International Conference on Intelligent Robots and Systems*, San Diego, CA, pp. 3186-3190, 2007.

[6] H. Kwon, D. Rosario, N. Gupta, M. Thielke, D. Smith, P. Rauss, P. Gillespie, and N. Nasrabadi, "Hyperspectral Imaging and Obstacle Detection for Robotics Navigation" *U.S. Army Research Laboratory Technical Report #ARL-TR-3639*, September 2005.

[7] T. Hong, S. Legowik, and M. Nashman, "Obstacle Detection and Mapping System," *National Institute of Standards and Technology (NIST) Technical Report NISTIR 6213*, pp. 1-22, 1998.

[8] T. Hong, C. Rasmussen, T. Chang, and M. Shneier, "Fusing Ladar and Color Image Information for Mobile Robot Feature Detection and Tracking," *7th International Conference on Intelligent Autonomous Systems*, Marina Del Ray, CA, 2001.

[9] A. Rankin, L. Matthies, and A. Huertas, "Daytime water detection by fusing multiple cues for autonomous off-road navigation," *Proceedings of the 24th Army Science Conference*, Orlando, FL, November 2004.

[10] A. Rankin and L. Matthies, "Daytime water detection and localization for unmanned vehicle autonomous navigation," *Proceedings of the 25th Army Science Conference*, Orlando, FL, November 2006.

[11] T. Yao, Z. Y. Xiang, J. L. Liu, and D. Xu, "Multi-feature fusion based outdoor water hazards detection," *Proceedings of the IEEE Conference on Mechatronics and Automation*, pp. 652-656, 2007.

[12] T. Yao, Z. Xiang, and J. Liu, "Robust water hazard detection for autonomous off-road navigation," *Journal of Zhejiang University*, 10(6), pp. 786-793, 2009.

[13] M. Fischler, C. Connolly, and R. Bolles. Unpublished work performed during the U.S. Army Research Laboratory funded Robotics Collaborative Technology Alliances program by SRI International, Menlo Park, CA, 2004.

[14] A. Rankin, M. Bajracharya, A. Huertas, A. Howard, B. Moghaddam, S. Brennan, A. Ansar, B. Tang, M. Turmon, and L. Matthies, "Stereo-vision based perception capabilities developed during the Robotics Collaborative Technology Alliances program," *Proceedings of SPIE*, Vol. 7692, Orlando, FL, pp. 76920C1-76920C15, April 2010.